Green chemistry synthesis and structural and optical study of $Dy_2(CO_3)_3 \rightarrow Dy_2O_3$ transition

O. Portillo Moreno

Facultad de Ciencias Químicas, Benemérita Universidad Autónoma de Puebla, Av. 14 Sur Col Jardines de San Manuel, Ciudad Universitaria, Puebla, Pue., México, 72570, Puebla, México.

M. Chávez Portillo

Universidad Politécnica de Puebla, Juan C. Bonilla, Puebla México.

H. Juarez Santiesteban, J. Alvarado Pulidoc, and Y. Ramos Reynoso

Centro De Investigación en Dispositivos Semiconductores, del Instituto de Ciencias de la Universidad Autonóma de Puebla, Av. 14 Sur Col Jardines De San Manuel, Ciudad Universitaria, Puebla, Pue., México

L. Serrano de la Rosa

Instituto de Física, Benémerita Universidad Autónoma de Puebla, J-48, Puebla, Puebla 72570, México.

Received 13 June 2022; accepted 1 August 2022

This paper presents preliminary results of $Dy_2\,(CO_3)_3 \rightarrow Dy_2O_3$ transition have been successfully obtained by Chemical Bath Deposition technical and subsequent thermal annealing temperature at $\sim 600^{\circ}\mathrm{C}$. Two different temperatures of $\sim 20^{\circ}\mathrm{C}$ and $\sim 90^{\circ}\mathrm{C} \pm 2^{\circ}\mathrm{C}$ are chosen to carry out the nanocrystalline growth. The crystalline phase is investigated by X-Ray Diffraction (XRD) and some optical properties; Transmittance, Reflectivity, Normalized Absorbance, real (n) and imaginary (k) parts refractive index. The crystalline phase of these inorganic nanomaterials for $Dy_2\,(CO_3)_3$ is orthorhombic phase, while for Dy_2O_3 it is cubic. Grain size average values located at ranged $2.8 - 3.4\,\mathrm{nm}$ for $Dy_2\,(CO_3)_3$ and $\sim 6.5 - 9.6\,\mathrm{nm}$ for Dy_2O_3. Vibrational modes are identified by Raman spectroscopy, modes at $\sim 150 - 1800\,\mathrm{cm}^{-1}$ frequency range assigned to internal vibrations of CO_3^{2-} ion: v_{1-} symmetric stretching $\left(\sim 1098\,\mathrm{cm}^{-1}\right)$ V_3-asymmetric $-C-O$ stretching situated at $\sim 1063\,\mathrm{cm}^{-1}$, were observed corresponding to orthorhombic crystalline phase. The $F_g + A_g$ and $A_{1\,g}$ modes, corresponding to cubic phase Dy_2O_3. Absorption measurement were assigned to the transitions from ground state $\left({}^6H_{15/2)}\right.$ to different excited states such as ${}^4I_{13/2} \rightarrow {}^4F_{7/2}, {}^4I_{15/2}, {}^6F_{3/2}, {}^6F_{5/2}, {}^6F_{7/2} \rightarrow {}^6H_{5/2}, {}^6F_{9/2} \rightarrow {}^6H_{7/2}, {}^6F_{11/2} \rightarrow {}^6H_{9/2}$ and ${}^6H_{11/2}$ of Dy^{3+} cation. Tauc's plot reveals band gap situated at range $\sim 4.66 - 5.17\mathrm{eV}$ for $Dy_2\,(CO_3)_3$ and $\sim 4.26 - 4.80\mathrm{eV}$ for Dy_2O_3 respectively.

Keywords: Dysprosium; absorption bands; crystalline phase; grain size; nanomaterials.

DOI: https://doi.org/10.31349/RevMexFis.69.021302

1. Introduction

Dysprosium (Dy) is an element that belongs to the rare earth classification, it has the [Xe] $4f^{10}6s^2$ electronic configuration. This rare earth combines with the carbonate $\left(CO_3^{2-}\right)$ ion under suitable conditions, thus generating dysprosium dioxymonocarbonate $Dy_2\,(CO_3)_{3(\,s)}$ [1]. Considered the broad search applied at high-performance luminescent devices, photocatalysts, etc., associated at electronic and optical, and structural properties arising of the $4fs \rightarrow 4fs$ electronic intra-transition, it is possible to carry out detailed studies of this nanomaterial. Have been investigated due to their optical and structural properties, for which they are important with high potential associated with the wide range of applications [2]. Here, are some of the $Dy_2\,(CO_3)_{3(\,s)}$ synthesis techniques: using ammonium bicarbonate as a precipitant [3], gravimetrically [4], sonochemical [5], via an amorphous precursor [6], among other interesting techniques, both chemical and physical [7]. Another inorganic nanomaterial that contains Dy^{3+} cation in its crystal structure is dysprosium oxide (Dy_2O_3), which has been prepared by the following techniques; Vacuum Sintering [8], Rapid thermal annealing [9], Atomic Layer Deposition [10]. Because of its thermodynamic stability relative, $Dy_2O_{3(\,s)}$ is considered a suitable nanocrystal for resisting corrosion in stainless steels at elevated temperature, is employed in microelectronic devices such as resistive switching devices [11]. It is important to point out that of the immense and overwhelming variety of synthesis techniques, it is sought to apply some that are simple and also nonpolluting, with the aim of obtaining nanomaterials at a relatively low cost. Despite the advantages of green synthesis, current methods face challenges with appropriate solvent selection, reaction temperature, reagents process chemical parameters that affect the synthesis process [12]. Here, we apply the green technique or Chemical Bath Deposit (CBD) in which the parameters of crystalline growth are easily controlled [13,14,15]. And so, we report a simple method for prepare $Dy_2\,(CO_3)_{3(\,s)}$ powder, and subsequent thermal annealing temperature (TT) in air atmosphere at $\sim 600^{\circ}\mathrm{C}$

to study $Dy_2(CO_3)_{3(a)} \rightarrow Dy_2O_{3(s)}$ transition. In this manuscript, we demonstrated that $Dy_2O_{3(s)}$ could be successfully prepared by CBD technique from $Dy_2(CO_3)_{3(s)}$ and it was worth noting that the size of $Dy_2O_{3(s)}$ nanocrystals could be easily controlled by adjusting the synthetic parameters. In addition, the effects of some optical and structural properties on $Dy_2(CO_3)_{3(a)} \rightarrow Dy_2O_{3(s)}$ transition, were examined. We believe that this manuscript will bring a novel strategy to synthesis of $Dy_2(CO_3)_{3(s)}$ and $Dy_2O_{3(s)}$ nanocrystals. $Dy_2O_{3(s)}$ it highly suitable for applications, such as in filters, modulators, switches, and anti-reflection coatings [16]. Due to the interesting optical properties of these nanomaterials, it is possible to investigate in detail the $4fs \rightarrow 4fs$ electronic intra-transitions located at UV-Vis-IR region, associated at Dy^{3+} cation. These are generally, reflectance $(\%R)$, Transmittance $(\%\,T)$ percentage and Absorbance, which have been examined. The analysis of the chemical kinetics of crystalline growth is carried out in the key stage and is based on the experimental synthesis applying the green chemistry or CBD technique. This paper presents preliminary results of crystalline growth in synthesizing inorganic materials to analyze the chemical equilibria in the growth of $Dy_2(CO_3)_{3(s)}$ nanocrystals, which is carried out in aqueous solution with pH alkaline (~ 8.3), the parameters remain constant during the evolution of the chemical equilibria except the reaction temperature. Two reaction temperatures are systematically chosen, $\sim 20°C$ and $\sim 90\,°C \pm 2°C$. A systematic study of the optical and structural properties are considered. The presentation of chemical kinetic equilibria are generally key parameters to achieve the expected chemical product. This is done in principle in order to find the correlation of the proposed chemical kinetic mechanism with the structural properties and these in turn with the optical ones.

2. Chemical reactions and experimental procedure

The crystalline growth of $Dy_2(CO_3)_{3(s)}$ nanocrystals is systematically prepared by CBD green technique and the theoretical experimental model is proposed as a first approximation, in a comprehensive manner according to the key stages previously presented [13,14,15,17]. A parameter of interest associated with the crystalline growth of nanoparticles in the solid phase is related to the van der Waals forces present in the aqueous solution in which the positive and negative ions are found. On other hand, the electrostatic van der Waals interactions associated with anions and cations [18]. A systematic study of the different electrostatic interactions in crystal growth is necessary for a better understanding of the chemical kinetic phenomenon [19]. It also shows charged and polar species through forming ion pairs, and other electrostatic interactions, which favor the creation of strong chemical bonds. The electrostatic interactions are complex because they depend on the molecular environment associated with the geometric distribution of the charge of the ion-cation and the symmetry of the electrostatic charge that surrounds the chemical species which is in equilibrium in some cases due to electrostatic interaction of the solvent and the ionic species. The energetic polarization of the ionic species (ions and cations, including the solvent) present in the aqueous solution correlates linearly with the magnitude of the electric field, which is difficult to predict exactly and is still under study [20]. For the kinetic mechanism considered here by us, the carbonate $\left(CO_3^{2-}\right)$ ion has been identified in aqueous solution through FT-IR studies, hydrolysis of thiourea $SC(NH_2)_2$ generates CO_3^{2-}, ion an NH_3 molecules [13,15,21]

$$SC(NH_2)_2 + 3H_2O \Leftrightarrow CO_3^{2-} + HS^- + 3NH_3.$$

Here, we present a brief and simple exposition of the chemical properties of CO_3^{2-} and OH^- ions, with the aim of interpreting in a simple way the interactions in the formation of the chemical bonds and the synthesis of $Dy_2(CO_3)_{3(s)}$ nanomaterial. The Lewis ionic molecular structure of CO_3^{2-} ion, electronic delocalization structure has three π bonds (π bond, sp^2 hybridization) [22]. The CO_3^{2-} ion is found to show an ionic arrangement with trigonal molecular geometry in which the central carbon atom is surrounded by three oxygen (O^{2-} ions) with plane geometry. The configurational phenomenon typical in organic and inorganic molecules with conjugated double π-bonds and in turn, associated with π-resonance. In the molecular design of π-conjugated systems has been investigated. This physicochemical behavior and relative thermodynamic stability, which in principle quantitatively allows us to understand the different chemical equilibria associated with the products obtained [23]. We found in preliminary reports, rare earths cations prepared by CBD technique, present the following order OH^- and CO_3^{2-} of capture (under the same experimental conditions of chemical synthesis); $Sm(OH)_3 < Ho(OH)_3 < NdOHCO_3 < ErOOH < CeO_2$ [14,15,25,26]. This capture order is linked to properties associated with electron affinity, ionic radii, electronegativity, to mention just a few of these intrinsic characteristics, and requires formal study. In aqueous solution, CO_3^{2-} ion exist together in a dynamic equilibrium relative and carbon dioxide $CO_{2(aq)}$ soluble in water; which presents the thermodynamic equilibrium through the conversion to carbonic acid $H_2CO_{3(aq)}$. The acid-base HCO_3^- equilibria, and the transport of electric charge from one species to another is complex and requires care since it formally depends on the medium and/or the type of solvent that it's difficult to understand them without a quantitative model [27,28]. Tentatively, in crystal growth we propose that the alkaline medium, ionic radii, electronic affinity and synthesis conditions, of capture of $OH^-$and CO_3^{2-} ions are crucial in obtaining the corresponding hydroxide and/or carbonate [14,15,25,26,29].

The equilibria in this acid-base system are shown below, without losing sight of the fact that they depend on the acid-base aqueous medium.

$$HCO_3^- + H_2O \rightarrow CO_3^{2-} + H_3O^+$$
$$HCO_3^- + OH^- \rightarrow CO_3^{2-} + H_2O.$$

The ion exchange process slowly generates the chemical phenomenon with ionic and molecular rearrangements associated with the slow and gradual capture of OH^-ion with simultaneous release of NH_3 molecules. In the initial stage, the $Dy(OH)_{3(aq)}$ are present, it releases OH^- ions and through molecular exchange with ligands (L) NH_3, created indirectly the coordination complex $[Dy\,(NH_3)_6]^{3+}$ cation. It is at a key stage in chemical synthesis since the importance of the type of molecule L and its properties associated with size, location of donor electron pairs, electronegativity, etc., of L are considered, these roles include small inorganic molecules with ability to complexate with tunable polarity to preferentially bind crystallographic domains, to mention just some of the multiple parameters associated with crystal growth [30]. The following equilibria associated with the acidity constant ($\Sigma \log K$) for species considered here, is the following sequence of acidic species reported, $\Sigma \log K = \log(k_1k_2k_3k_4) = -17.62 \pm 0.07$ [31].

$$CO_{2(g)} \overset{k_1}{\Rightarrow} CO_{2(aq)} \overset{k_2}{\Rightarrow} H_2CO_{3(aq)} \overset{k_3}{\Rightarrow} HCO_3^- + OH^- \overset{k_4}{\Rightarrow} CO_3^{2-}.$$

The complex of coordination $[Dy\,(NH_3)_6]^{3+}$ cation, the following chemical equilibria is proposed. Here, we consider the key stage associated with the chemical kinetic mechanism in the chemical synthesis of the product. Parameters chemical such as pH, molecular hydration of the L, stirring, temperature and nucleation time and their implication in the study of such precipitation processes will be investigated [32].

$$Dy^{3+} + 3OH^- \rightarrow Dy(OH)_{3(aq)}$$
$$Dy(OH)_{3(aq)} + 6NH_3 \Leftrightarrow [Dy\,(NH_3)_6]^{3+} + 3OH^-$$
$$2\,[Dy\,(NH_3)_6]^{3+} + 3CO_3^{2-} \rightarrow Dy_2\,(CO_2)_{3(s)} + 6NH_3 \quad (\Delta G^0) = -780.06\ \text{kcal/mol}$$

According to the negative sign (-) of ΔG^0, it is found that the probable and spontaneous thermodynamic equilibrium According to the chemical equilibria presented previously, the kinetics of the crystalline growth of $Dy_2\,(CO_3)_{3(\,s)}$ and $Dy(OH)_{3(\,s)}$ nanocrystals

$$3\,[Dy\,(NH_3)_6]^{3+} + 3OH^- \rightarrow Dy_2\,(CO_2)_{3(s)} + 6NH_3 + Dy(OH)_{3(\,s)}.$$

We mention the key chemical and physical parameters associated with crystalline growth (i) nucleation and particle growth, the clusters formed undergo rapid decomposition and growth within the context of rare earth nanocrystal synthesis [33,34], (ii) then the particles combine to grow up to nanopowder. (iii) The particles distribution becomes remarkably narrow during the first stages of coarsening and progressively turns to a small crystal time passes.

2.1. Experimental part

2.1.1. Preparation of the powders

The experimental details associated with the crystal growth parameters applying the green (CBD) technique, have been previously reported [14,15,17,21,24-26,28]. Now, a brief report is presented considering only the most relevant experimental details for crystal growth. Preparation of $Dy_2\,(CO_2)_{3(\,s)}$ nanopowders grown by CBD technique was performed at $20 \pm 2°C$ and $\sim 90 \pm 2°C$ temperature, $pH \sim 8.3$. Next, four solutions are prepared with deionized water ($\sim$ 18.2MΩ) containing the precursor reagents: Dysprosium nitrate $Dy\,(NO_3)_4 \cdot 5H_2O(0.2M)$, Potassium hydroxide $KOH(0.1M)$, Ammonium nitrate NH_4NO_3 $(1.2M)$ and thiourea $SC\,(NH_2)_2\,,(0.1M)$. The progenitor's reagents, were mixed in a 250 mL flat-bottomed beaker at room temperature and the final solution is a white precipitate, filtered and rinsed several times to remove impurities. The samples were labeled as Dy 20 and Dy 90, are dried at room temperature, ready for characterization. The thermal annealing treatment (TT) was carried out in a quartz tubular furnace with air, with normal pressure, at $\sim 600 \pm 5°C$ during 1.0 h. Now, the TT samples are labeled using the Dy 20 TT and Dy 90 TT symbology.

2.1.2. Experimental characterization techniques used

X-Ray Diffraction patterns were registered in a D8 Bruker. X-ray structure and data refinement were obtained from a 150(2)A Bruker Apex II CCD diffractometer using MoK_α radiation ($\lambda = 0.710$Å). The spinning samples were scanned over a 2θ range of $\sim 10 - 90°$ by steps of $\sim 0:02°$, with a time step of ~ 1.2 s. Experimental absorbance (α) results vs. wavelength (λ) were recorded using a Varian Cary 5000 UV-vis-NIR spectrophotometer, were carried out at range $\sim$ 200 − 2500 nm (6.20-0.49 eV. Micro Raman (Horiba), LabRAM HR, to identify the vibrational modes of our material.

3. Results and discussion

Figure 1a) shows the X-Ray Diffraction (XRD) diffractograms of (a) Dy 20 and Dy 90 (b) Dy 20TT and Dy 90TT samples. Different relative intensity and broadening in crystalline reflections are generally assigned at nanocrystals [13-15,17,24-6]. Here, four different crystalline reflections are observed in the Dy 20 sample, located at $2\theta \sim 19.89°, 29.71°, 46.16°$ and $\sim 50.97°$, while in the Dy

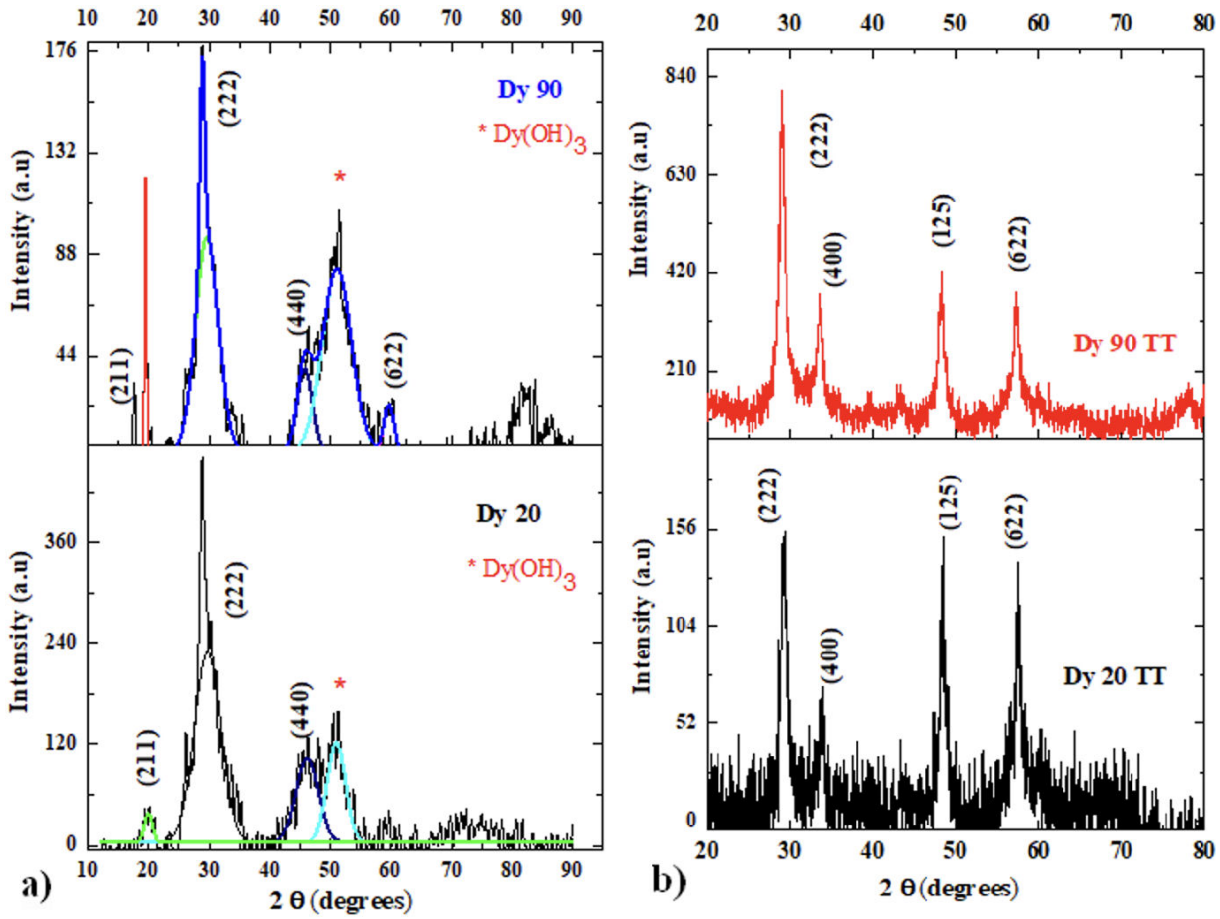

FIGURE 1. X-Ray Diffraction (XRD) diffractograms of a) Dy 20, Dy 90 and b) Dy 20 TT, Dy 90 inorganic nanocrystals.

90 nanomaterial, five reflections located at angular positions $2\theta \sim 19.46°, 29.59°, 45.77°, 55.08°$ and $59.67°$, respectively. The reflections correspond to those of the lanthanide-type rare-earth carbonates, and all the reflections can be indexed in the orthorhombic system [35], both nanomaterials are identified to $Dy_2(CO_2)_{3(s)}$ nanomaterial, which is in agreement with Niasari *et al.* [5] and Nasrabadi1 *et al.* [2]. However, the plane crystalline located at $2\theta \sim 51.0°$ (is indicated in the diffractogram by an asterisk in the upper part of the crystalline plane) can be readily indexed to a pure hexagonal phase of Dysprosium hydroxide $Dy(OH)_3(JCPDS19-0430)$ [36]. A particular structural characteristic of nanomaterials is associated with the gradual widening and relative decrease in the crystalline planes, a situation here observed in our chemical compounds. A particular and important feature of the structural behavior of organic and inorganic materials is related to: crystalline stacking faults, grain boundaries, stoichiometry, and in general the intrinsic native crystalline defects, which are related in principle with the widening and decrease of the crystalline planes that inevitably originate during crystalline growth [36]. According to the experimental XRD diffraction patterns, it is possible to observe that a crystalline plane is oriented at (222) direction in both nanomaterials with TT and without TT, respectively, associated with the experimental conditions of synthesis and requires a deep and detailed study applying a suitable theoretical model. The preferred orientation and this is associated with the symmetrical structural part of the ionic and/or molecular packing. We discussed this structural phenomenon in a preliminary way in some previous reports for organic and inorganic nanocrystals [13,37,38]. The plane of lower relative crystalline energy is favored by optimal chemical and physical parameters, is generated by various parameters of crystalline growth related and plausibly raised considering ionic packing, which reaches a relative energy minimum [39]. However, the occurrence of these structural types appears to be random with no rules governing their structural formation. As a first approximation to these XRD experimental results, we deemed that, according to the reflections plane observed, structural symmetry associated as a result of the presence of the stereogenic carbon atom $\left(CO_3^{2-}\right)$. In aromatic compounds, the molecular stability originates from the π-resonance effect [40]. The surface energy of the nanocrystals, is a relevant property of a crystal that is crucial to the understanding of various structural phenomena like surface segregation, roughening, catalytic activity, and the crystal's equilibrium shape [41]. The main parameters affecting the structural properties, such as size, shape, concentration of nanoparticles, aggregation, are

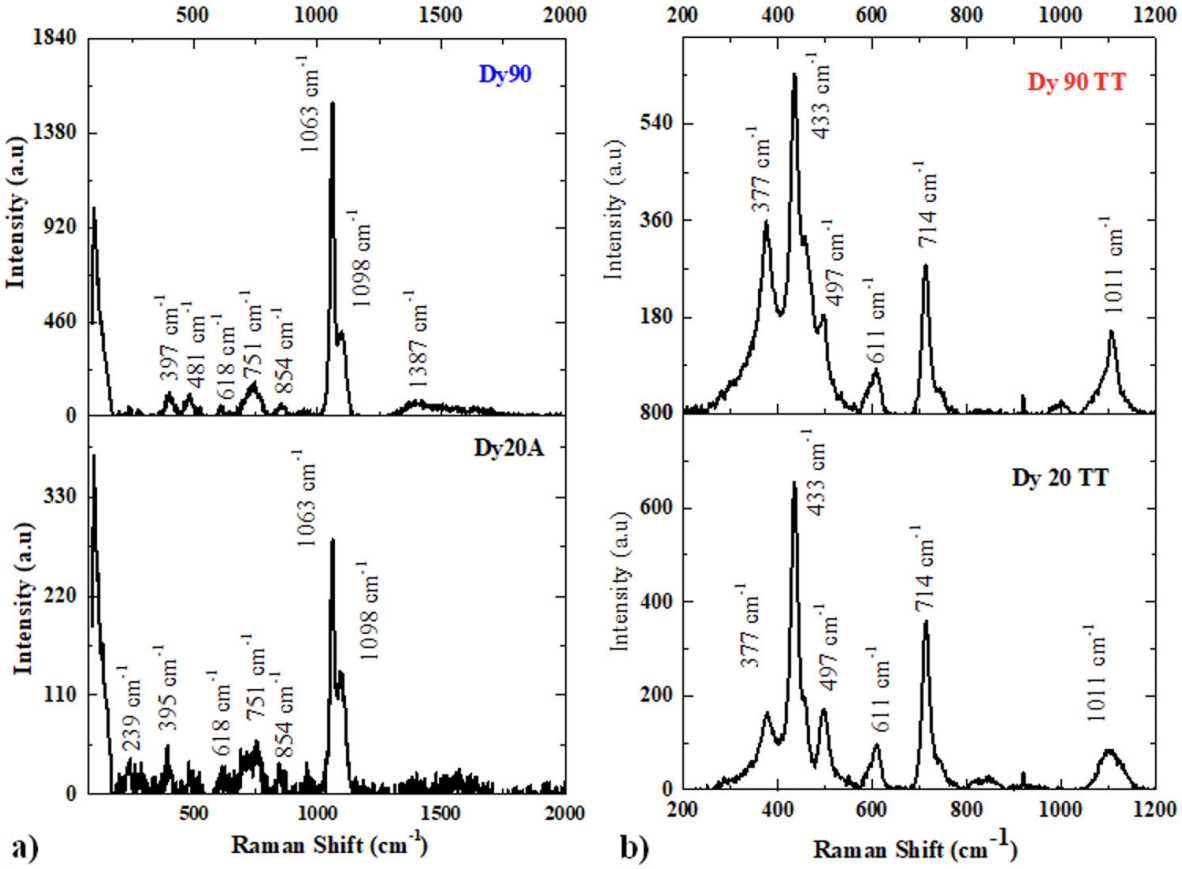

FIGURE 2. Raman spectra of a) Dy 20 and Dy 90, b) Dy 20 TT and Dy 90 TT nanocrystals.

TABLE I. Compilation of the numerical values of the average grain size GS (nm) and the FWHM of Dy 20 and Dy 90 samples.

Dy 20			Dy 90		
2θ	FWHM	GS (nm)	2θ	FWHM	GS(nm)
19.89	2.34	3.44	19.46	0.37	21.78
29.71	2.32	3.54	29.59	2.85	2.88
46.16	3.01	2.86	45.77	2.21	3.90
50.97	3.25	2.70	51.08	3.15	2.79
...	...	...	59.67	1.58	5.79

TABLE II. Compilation of the numerical values of the average grain size (GS) and the FWHM of Dy 20 TT and Dy 90 TT samples.

Dy 20 TT			Dy 90 TT		
2θ	FWHM	GS (nm)	2θ	FWHM	GS (nm)
29.27	0.905	9.0	29.03	0.92	8.9
33.79	0.857	9.6	32.93	0.84	9.8
48.46	0.904	9.6	48.25	0.81	10.7
57.47	1.379	6.5	57.27	1.03	8.7

of interest to understand the optical behavior. We consider that some nanomaterials show the aforementioned preferential orientation, which is tentatively associated with the slow stirring of the solution containing the progenitor reagents and the long reaction time in crystal growth. The XRD of Dy 20 TT and Dy 90 TT samples are shown in Fig. 1b), according to (JCPDS Card No. 86-1327) in cubic bixbyite phase of $Dy_2O_{3(s)}$ cubic phase is identified and no other reflections exists [42]. Both inorganic materials have the same cubic crystalline phase and preferential orientation of the (222) reflection. The effect of TT on Dy 20TT and Dy 90TT inorganic nanocrystals, can be understood according to the following plausible chemical reaction $Dy_2(CO_2)_3 \overset{\sim 600^\circ C}{\Longrightarrow} Dy_2O_{3(s)} + 3CO_{2(g)} \uparrow$.

The grain size (GS) average is quantified numerically using the Scher $GS = k\lambda/\beta\cos\theta$ eq., were λ is the wavelength of X-ray radiation (~ 0.154Å), k the Scherer's constant $(k \sim 0.9), \theta$ (in radians) the characteristic X-ray radiation and β is the Full Width at Half-Maximum (FWHM) of the crystalline plane (in radians). A set of physical parameters characterizes the nanocrystals: size, shape, structure, and optical properties to find some correlation between these. Table I and II presents a compilation of the numerical values of the mean grain size (GS) and the FWHM of Dy 20, Dy 90 and Dy 20 TT, Dy 90 TT samples. The numerical average value reported here for the GS of the nanocrystals is located at $\sim 2.32\ 3.25$ nm for the Dy 20 sample and $\sim 2.79-21.78$ nm in the case of Dy 90 nanocrystal, respectively.

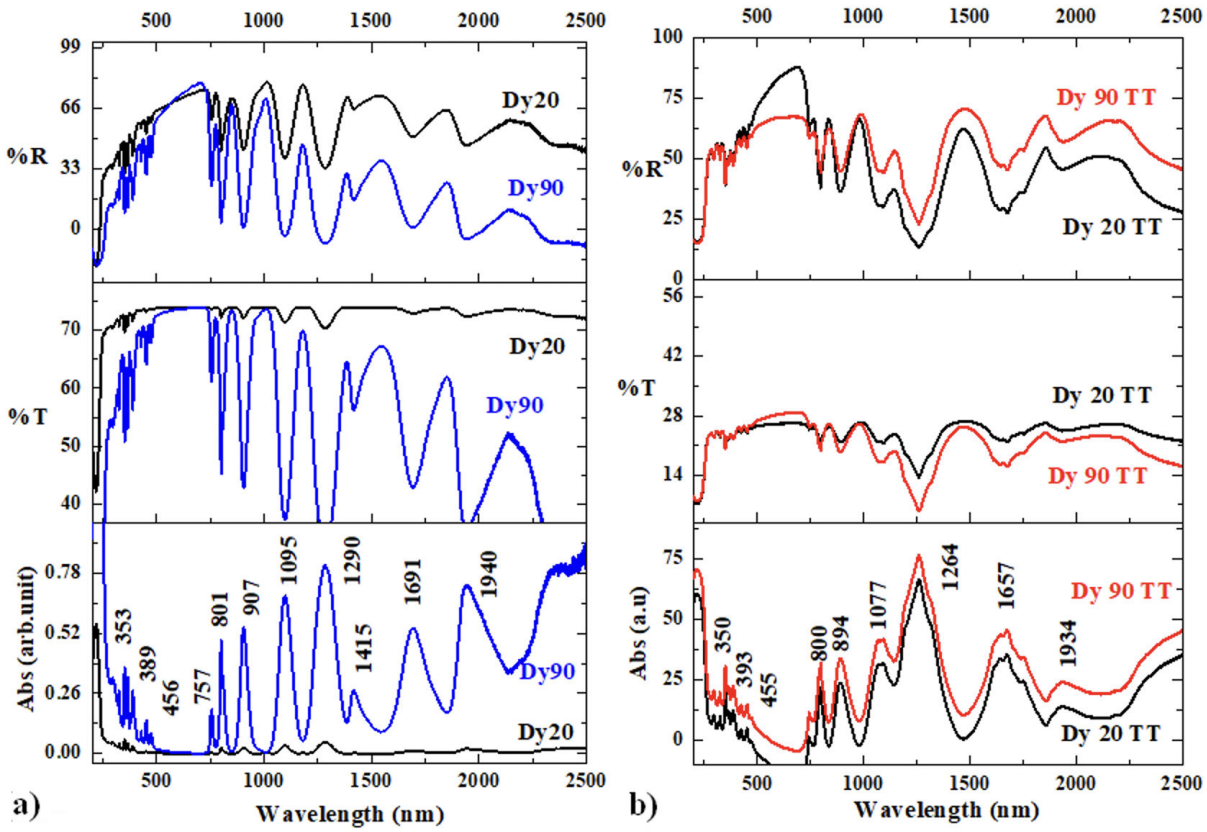

FIGURE 3. UV-Vis spectra of a) Reflectance $(\%\mathrm{R})$, b) Transmittance (%T) and c) absorbance vs. $\lambda(\mathrm{nm})$ of Dy 20, Dy 90, Dy 20 TT and Dy 90 TT nanocrystals, respectively.

Raman analysis was carried out for all samples. Figure 2 shows Raman spectra of (a) Dy 20 and Dy 90, (b) Dy 20 TT and Dy 90 TT nanocrystals. Four bands located at $\sim 150 - 1800\,\mathrm{cm}^{-1}$ frequency range assigned to internal vibrations of CO_3^{2-} ions: v_1-symmetric stretching $\left(\sim 1098\,\mathrm{cm}^{-1}\right)$ v_3-asymmetric -C-O stretching at $\sim\ 1063\,\mathrm{cm}^{-1}$, were observed. The vibrational mode are shifted to slightly higher wavenumbers when compared to the vibrational mode in CO_3^{2-} pure, due to the inner-sphere coordination of Dy^{3+} cation with CO_3^{2-} ligands (L). The frequencies for the vibrational mode of CO_3^{2-} ion situated at $\sim 1063\,\mathrm{cm}^{-1}$ and $\sim 1415\,\mathrm{cm}^{-}\,1$, are assigned when the first two modes nondegenerate. Lattice vibrational mode, V_{3-} asymmetric -C-O stretching $\left(\sim 1063\,\mathrm{cm}^{-1}\right)$, v_1-symetric $\mathrm{O}-\mathrm{C}-\mathrm{O}$ stretching $\left(\sim 1098\,\mathrm{cm}^{-1}\right)$, and the intensity of the v_{14} band, associated with lattice vibration parallel to the $\boldsymbol{c}$-axis, correspond to the in-plane bending (v_4) of $-\mathrm{C}-\mathrm{O}$, out-of-plane bending (v_2) of $\mathrm{O}-\mathrm{C}-\mathrm{O}$, doubly degenerate asymmetric stretching (v_3) of $\mathrm{O}-\mathrm{C}=\mathrm{O}$, and the overtone of the out-ofplane bending mode $(2\mathrm{v}_2)$ vibrations, respectively [43]. The splitting of the nondegenerate bands is generally an indication of nonequivalent CO_3^{2-} ions [44]. Three weak Raman vibrational mode were found and assigned to A_g, E_{2g} and E_{1g} liberation modes. A vibrational spectrum of intra-and inter-metal and semimetal bonds study using Raman spectroscopy complexes of $\mathrm{Ln}-(\mathrm{OH})_3$ with symmetry analysis and vibrational mode assignments [45]. The primary vibrational mode in the solid phase for $\mathrm{Dy(OH)}_{3(\mathrm{\ s})}$ occur at $\sim 397\,\mathrm{cm}^{-1}$ and that the vibrational mode are sharp and relatively narrow bands. The spectrum for Dy 20 and Dy 90 samples exhibit vibrational mode in the regions near those reported for $\mathrm{Dy(OH)}_3$. The sharp vibrational mode situated at $\sim\ 1040\ -\ 1060\,\mathrm{cm}^{-1}$ result from the coordinated $CO_3^{2-}\mathrm{L}$ [4]. Raman spectrum of Dy 20 and Dy 90 nanocrystals shows for active vibrational modes that would indicate that O4 is a coordinated $-\mathrm{OH}$ ion. Metal hydroxides (M-OH) typically exhibit active Raman vibrational mode and deformation modes below $\sim 1200\,\mathrm{cm}^{-1}$, the observed average shift may be attributed to size effects or surface stress/strain [46]. For the Dy 20 TT and Dy 90 TT nanocrystals obtained, strong Raman vibrational modes were observed at $\sim 377\,\mathrm{cm}^{-1}$, which were assigned to the $\mathrm{F_g}$ mode [47]. The cubic phase was implied by the strong Raman intensity vibrational modes, with a large charge of polarizability appearing during the vibration. Raman active region and $\mathrm{Dy_2O_{3(\ s)}}$ cubic phase were in good agreement with previously published evidence [48]. Raman vibrational mode at $\sim 477\,\mathrm{cm}^{-1}$ and $\sim 611\,\mathrm{cm}^{-1}$ were assigned to the combination of $(\mathrm{F_g}+\mathrm{A_g})$ stretching vibration modes. For the C-type $\mathrm{Dy_2O_3}$ with a space group of Ia-3, the irreducible representations were ascribed to $4\,\mathrm{A_g}+4\mathrm{E_g}+14\,\mathrm{F_g}+5\,\mathrm{A_{2u}}+5\mathrm{E_u}+16\,\mathrm{F_u}$, where $\mathrm{A_g}$, $\mathrm{E_g}$, and $\mathrm{F_g}$ are Raman active [49]. The Raman vibra-

tional mode of the Dy 20TT and Dy 90 TT samples, shows a higher crystallinity due TT effect. The bridged oxygen modes band situated at range $\sim 300-600\ \mathrm{cm}^{-1}$ region includes the bands at $\sim 377\ \mathrm{cm}^{-1}$ and $\sim 477\ \mathrm{cm}^{-1}$ of Dy-O characteristic vibration [50], illustrating the $\mathrm{F_g} + \mathrm{A_g}$ and $\mathrm{A_{1\ g}}$ modes, respectively of cubic phase $\mathrm{Dy_2O_{3(\ s)}}$ [51].

Figure 3 displays the UV-Vis (a) Reflectance $(\%\mathrm{R})$, (b) Transmittance (%T) and (c) absorbance vs. wavelength (λ) spectrum of Dy 20, Dy 90, Dy 20 TT and Dy 90 TT. According to the optical behavior of $(\%\mathrm{R}), (\%\ \mathrm{T})$ and absorbance, let's divide the graph into three different regions. The optical spectral of Dy 20 and Dy 90 , the $\%$ T located at two regions is directly observed. Examining the optical behavior in the $\%\mathrm{R}$ spectra, we have the following: at $\lambda \sim 200-750\ \mathrm{nm}$ $(\sim\ 6.20-1.65\mathrm{eV})$, the $\%\mathrm{R}$ shows an increase with the $\lambda(\mathrm{nm})$ until reaching a relative maximum of $\sim 68\%$, for Dy 20, Dy 90 and Dy 20 TT, Dy 90 TT of $\sim 75\%$. An increase in the $\%\mathrm{R}$ is appreciated, which is associated with the effect of the TT with the structural properties of inorganic materials [52,53]. For located at range $\lambda \sim 750\ 1750\ \mathrm{nm}(\sim 1.65-0.70\mathrm{eV})$, shows oscillatory optical behavior of $\%\mathrm{R}$, with several relative maximums/minimum situated at range $\sim 100-20\%$, at $\sim 1750-2500\ \mathrm{nm}(\sim 0.7-0.04\mathrm{eV})\%\mathrm{R}$ shows two isolated relative maximum, which decreases up to $\sim 20\%$. UV-Vis region $(\lambda \sim 200-750\ \mathrm{nm})$, it shows an increase until reaching the relative maximum of $\sim 70\%$. Next, the %T shows oscillatory behavior with bands associated with $4fs \rightarrow 4fs$ electronic intratransitions, related at electron configuration [Xe] $4f^9 6s^0$ of Dy^{3+} cation. The in-line $\%$ T curves of Dy 20 TT and Dy 90 TT samples, decreases, which is due to the incomplete grain growth observed and weak agglomeration of nanocrystals caused by the surface energy will lead to different grain boundary migration rate at crystal growth. The nanocrystals show the transparency, and their in-line %T reach $\sim 70.0\%$ at $\geq 800\ \mathrm{nm}$, For Dy 20 TT and Dy 90 TT samples, the optical behavior of $\mathrm{R}\%$ and $\mathrm{T}\%$, is generally associated with $4f\ \mathrm{s} \rightarrow 4f\ \mathrm{s}$ electronic intra-transitions from one material to a different one, typical of TT materials [54]. Both nanomaterials, oscillatory behavior of $\mathrm{R}\%$ and $\mathrm{T}\%$ located at UV-Vis region situated at range $\sim 300-800\ \mathrm{nm}(\sim 4.13-1.55\mathrm{eV})$ can be seen, which is identified with $4fs \rightarrow 4fs$ electronic intra-transitions corresponding to rare earths. The absorbance spectrum show absorption bands (AB) situated at $\lambda(\mathrm{nm})$ and energy (eV) of $\sim\ 353\ \mathrm{nm}(\sim\ 3.51\mathrm{eV}), \sim 389\ \mathrm{nm}(\sim\ 3.18\mathrm{eV}), \sim\ 457\ \mathrm{nm}(\sim\ 2.71\mathrm{eV}), \sim\ 801\ \mathrm{nm}(\sim 1.54\mathrm{eV}), \sim 907\ \mathrm{nm}(\sim 1.36\mathrm{eV}), \sim 1095\ \mathrm{nm}\ (\sim 1.13\mathrm{eV}), \sim 1290\ \mathrm{nm}(\sim\ 0.96\mathrm{eV}), \sim\ 1415\ \mathrm{nm}(\sim\ 0.87\mathrm{eV}), \sim\ 1691\ \mathrm{nm}(\sim 0.73\mathrm{eV})$ and $\sim 1940\ \mathrm{nm}(\sim 0.63\mathrm{eV})$. They are generally assigned to $4fs \rightarrow 4fs$ electronic intra-transitions of Dy^{3+} cation, at the ground state $\left({}^6\mathrm{H}_{15/2}\right)$ into different excited states $\left({}^6\mathrm{P}_{7/2}\right)$,$\left({}^4\ \mathrm{F}_{7/2}\right)$, $\left({}^4\mathrm{I}_{15/2}\right)$, $\left({}^4\ \mathrm{F}_{9/2}\right)$, $\left({}^6\ \mathrm{F}_{3/2}\right)$, $\left({}^6\ \mathrm{F}_{5/2}\right)$, $\left({}^6\ \mathrm{F}_{7/2}\right)$, $\left({}^6\ \mathrm{F}_{9/2} + {}^6\mathrm{H}_{7/2}\right)$, $\left({}^6\ \mathrm{F}_{11/2} + {}^6\mathrm{H}_{9/2}\right)$ and $\left({}^6\mathrm{H}_{11/2}\right)$, respectively [55,56]. The AB were assigned to the electronic intra-transitions from ground state $\left({}^6\mathrm{H}_{15/2}\right.$ to different excited states such as ${}^4\mathrm{I}_{13/2} \rightarrow {}^4\ \mathrm{F}_{7/2}, {}^4\mathrm{I}_{15/2}, {}^6\ \mathrm{F}_{3/2}, {}^6\ \mathrm{F}_{5/2}$, $6\ \mathrm{F}_{7/2} \rightarrow {}^6\mathrm{H}_{5/2}, {}^6\ \mathrm{F}_{9/2} \rightarrow {}^6\mathrm{H}_{7/2}, {}^6\ \mathrm{F}_{11/2} \rightarrow {}^6\mathrm{H}_{9/2}$ and ${}^6\mathrm{H}_{11/2}$ of Dy^{3+} cation. The AB was observed at $\sim\ 1290\ \mathrm{nm}$, classified as hypersensitive electron intra transition for Dy^{3+} cation in optical spectra ${}^6\ \mathrm{F}_{11/2} \rightarrow {}^6\mathrm{H}_{15/2}$, at $\sim\ 1290\ \mathrm{nm}$ [55]. Some of the AB have disappeared at UV-region and are very sparse at $\sim 353\ \mathrm{nm}\left({}^6\mathrm{H}_{15/2} \rightarrow {}^6\mathrm{P}_{7/2}\right), \sim\ 389\ \mathrm{nm}\left({}^6\mathrm{H}_{15/2} \rightarrow {}^4\ \mathrm{F}_{7/2}\right)$ and $\sim\ 457\ \mathrm{nm}\ \left({}^6\mathrm{H}_{15/2} \rightarrow {}^4\ \mathrm{I}_{15/2}\right)$, and also they have very low intensity. The samples showed a hypersensitive intra-transition at $\sim\ 1290\ \mathrm{nm}\ \sim\ 0.96\mathrm{eV}\ \left({}^6\mathrm{H}_{15/2} \rightarrow {}^6\mathrm{H}_{11/2}\right)$ [57]. The $4f\ \mathrm{s} \rightarrow 4f\ \mathrm{s}$ hypersensitive intra-transition at $1290\ \mathrm{nm} \sim 0.96\mathrm{eV}\ \left(\mathrm{H}_{15/2} \rightarrow \mathrm{H}_{11/2}\right)$ [57]. The $4/5 \rightarrow 4/5$ and charge-transfer AB are observed for the most $4f_n$-series cations, the AB at Dy20 also, they have very low. Tentatively, according to this optical behavior, it is proposed that the dependence of free electron contribution to the dielectric function which can be the dependence of free electron contribution to the dielectric function which can be modified by changing at GS average. This statement is confirmed by our experimental results of XRD and the GS reported here. On the other hand, the optical phenomenon of the nanocrystal surface causes the Coulombic restoring force on the electron cloud becomes weaker has been systematically investigated [58].

Figure 4 displayed Normalized Absorbance vs. E(hv) spectrum of (a) Dy 20 and Dy 90 (b) Dy 20 TT and Dy 90 TT, nanocrystals. The emission property of rare earth ions located at Visregion can be majorly attributed to their predominant non-hypersensitive and hypersensitive electronic intra-transitions. Optical and structural studies were investigated related to ${}^4\ \mathrm{F}_{9/2} \rightarrow {}^6\mathrm{H}_{13/2}$ electronic intra-transitions in Dy^{3+} cation being an electric dipole transition is greatly sensitive [55]. On the other hand, Dy^{3+} cation populate the ${}^4\ \mathrm{F}_{7/2}$ meta-stable state during rapid of non-radiative decay process due to the small energy gap energy between ${}^4\mathrm{I}_{15/2}$ and ${}^4\ \mathrm{F}_{9/2}$ electronic states [59]. The electronic intra-transitions of Dy^{3+} cation present in yellow or blue regions of ${}^4\ \mathrm{F}_{9/2} \rightarrow {}^6\mathrm{H}_{13/2}$ (electric dipole) and ${}^4\ \mathrm{F}_{9/2} \rightarrow {}^6\mathrm{H}_{15/2}$ (magnetic dipole), respectively [60]. The electronic intra-transitions of ${}^4\ \mathrm{F}_{7/2} \rightarrow {}^6\mathrm{H}_{13/2}$ is hypersensitive, while the intensity of electronic intra-transitions of ${}^4\ \mathrm{F}_{9/2} \rightarrow {}^6\mathrm{H}_{15/2}$ is not quite sensitive. Dy^{3+} cation has been acknowledged for its white light production, which is appropriate at an acceptable yellow $\rightarrow$ blue $(\mathrm{Y} \rightarrow \mathrm{B})$ intensity ratio. The absorption transition from the lower level $\left({}^6\mathrm{H}_{15/2}\right)$ into the various energy levels ${}^6\mathrm{H}_{11/2}, {}^6\ \mathrm{F}_{11/2} + {}^6\mathrm{H}_{9/2}, {}^6\ \mathrm{F}_{9/2} + {}^6\mathrm{H}_{7/2}, {}^6\ \mathrm{F}_{7/2}, {}^6\ \mathrm{F}_{5/2}$, ${}^4\ \mathrm{F}_{9/2}, {}^6\ \mathrm{F}_{3/2}, {}^4\mathrm{I}_{15/2}, {}^4\ \mathrm{F}_{7/2}$ and ${}^6\mathrm{P}_{7/2}$. Table III and IV, shows $4fs \rightarrow 4fs$ electronic intratransitions of Dy 90, Dy 20 and Dy 90 TT, Dy20 TT nanocrystals. The $5s$ and $5p$ orbitals provide shielding effects on the $4f$ s electrons, generating as an optical response an intense AB in the different cations of the rare earths. Intense AB have been identified: ${}^6\mathrm{H}_{15/2}$ (blue), ${}^6\mathrm{H}^{13/2}$ (yellow) and ${}^6\mathrm{H}_{11/2} \rightarrow {}^6\mathrm{H}_{9/2}$ (red). Besides, the samples showed a hypersensitive transition at $\sim 1290\ \mathrm{nm}(\sim 0.96\mathrm{eV}), {}^6\mathrm{H}_{15/2} \rightarrow {}^6\mathrm{H}_{11/2}$ with high inten-

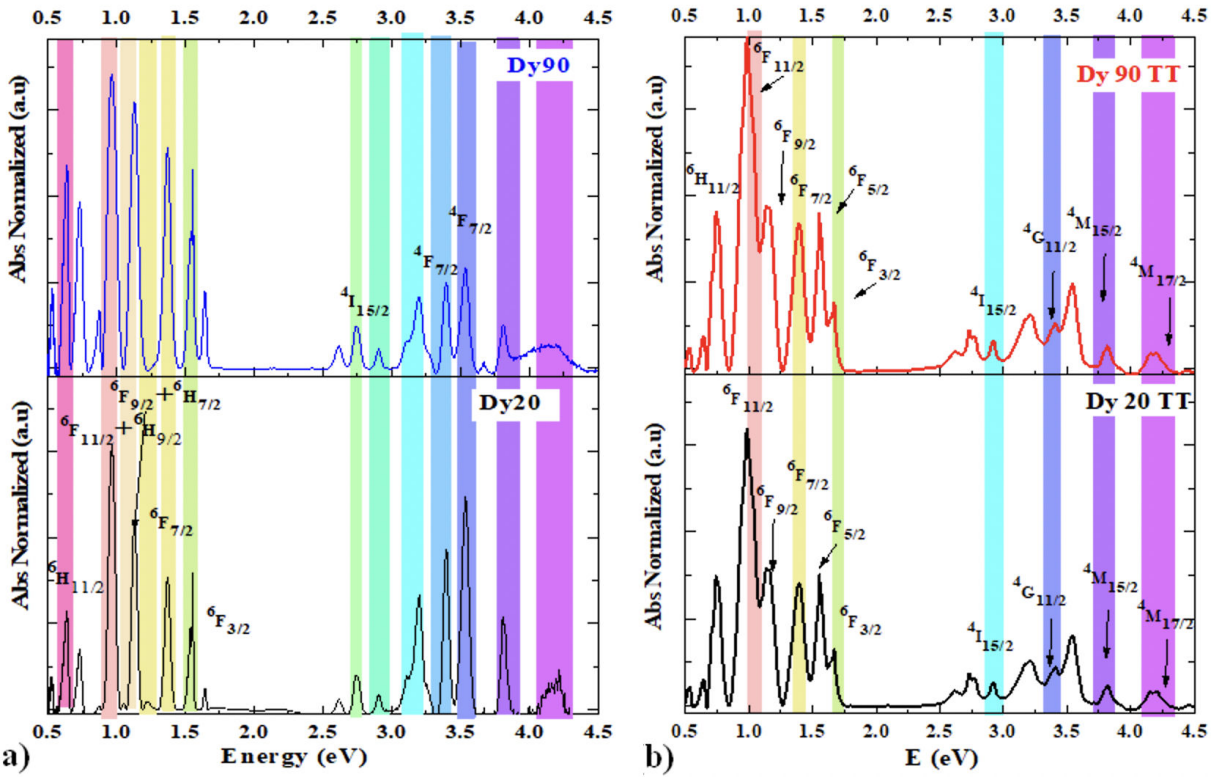

FIGURE 4. Normalized absorbance spectrum of (a) Dy 20 and Dy 90, (b) Dy 20 TT and Dy 90 TT nanocrystals. Table $3.4f \rightarrow 4f$ electronic intra-transitions of Dy 90 and Dy 20 nanocrystals.

sity [61]. with high intensity [61]. $Dy_2O_{3(\,s)}$ show AB located at $\sim 457\,\mathrm{nm}$ $(\sim 2.71\mathrm{eV})$, which were attributed to Dy^{3+} cation of ${}^4\,F_{9/2} \longrightarrow {}^6H_{15/2}$ electronic intra-transition [62]. The comparative analysis associated in principle with the chemical composition in the optical properties in these nanomaterials, in principle can be associated with the surrounding medium (atoms, molecules and ions), as well as intrinsic native crystal defects, stacking faults, grain boundaries, character of the stoichiometric balance, etc. These physicochemical parameters are observed and are generally assigned to changes in the optical properties of nanomaterials. The $-O-H, CO_3^{2-}$ ions, $-O-O=O$ and Dy^{3+} cation, generate molecular polarization through the photo-response to the interaction of the external incident radiation, the result of this optical phenomenon generates shift towards higher energy [63]. Those AB, especially those at the Vis-light range, may increase the sensitivity of the composition and are apt to be used in several applications such as sensors and solar cells.

Table IV $4f \rightarrow 4f$ electronic intra-transitions of Dy 20 TT and Dy 90 TT nanocrystals. Figure 5 displayed (a) the real (n) and imaginary (k) parts of refractive index vs. Wavelength of (a) Dy 20, Dy 90 and (b) Dy 20 TT, Dy 90 TT nanocrystals. The refractive index (n) vs. $\lambda(\mathrm{nm})$ of Dy 20, Dy 90 and 20 TT and Dy 90 TT samples. The electronic intra-transitions of greater relative intensity are seen in the Dy 20 and Dy 90 nanocrystals. The observed AB can, in principle, be justified by the optical and structural phenomena:

TABLE IV. $4f \rightarrow 4f$ electronic intra-transitions of Dy 20 TT and Dy 90 TT nanocrystals.

Absorption transition	$\lambda(\mathrm{nm})$	E(eV)
${}^6H_{15/2} \rightarrow {}^6P_{7/2}$	353 nm	3.51
${}^6H_{15/2} \rightarrow {}^6\,F_{7/2}$	389 nm	3.18
${}^6H_{15/2} \rightarrow {}^6I_{15/2}$	456 nm	2.71
${}^6H_{15/2} \rightarrow {}^6\,F_{15/2}$	801 nm	1.54
${}^6H_{15/2} \rightarrow {}^6\,F_{7/2}$	907 nm	1.36
${}^6H_{15/2} \rightarrow {}^6\,F_{9/2} + {}^6H_{15/2}$	1095 nm	1.13
${}^6H_{15/2} \rightarrow {}^6\,F_{11/2} + {}^6H_{9/2}$	1290 nm	0.96
${}^6H_{15/2} \rightarrow {}^6H_{11/2}$	1691 nm	–
${}^6H_{15/2} \rightarrow {}^6H_{11/2}$	1940 nm	...

$4fds \rightarrow 4fds$ electronic intra-transitions, native crystalline intrinsic defects as vacancies, grain boundaries, stacking faults, and stoichiometric and quantum confinement effect. It has been shown to a deviation of the local symmetry of the Dy^{3+} cation induced by the CO_3^{2-} and OH^-ion modifiers for O^{2-} ion, such differences in the optical properties arising from the 20TT and Dy 90TT samples electronic intra-transition. These ions were previously identified using the FTIR technique (they are not shown here) [13-15,17,24-26]. The properties of the nanocrystals can be assigned to the effects of quantum and electronic confinement. The AB intensity was found to increase with the concentration of the

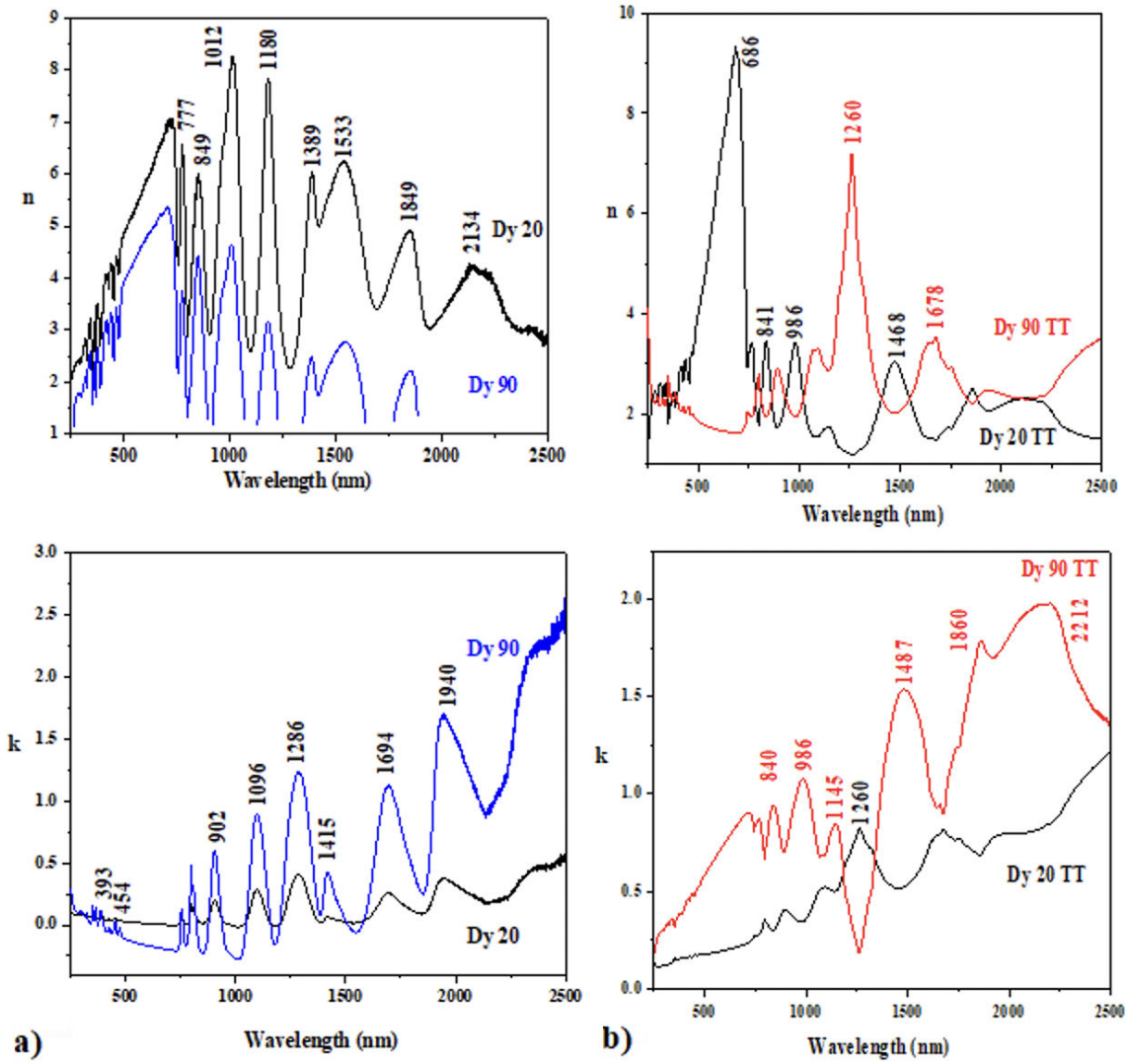

FIGURE 5. Real (n) and imaginary (k) parts of refractive index (n) vs. wavelength of a) Dy 20, Dy 90 and b) Dy 20 TT, Dy 90 TT nanocrystals.

CO_3^{2-} and OH^- ion. It can be related to the decrease in GS causes more atoms to be closer to the surface and thereby increasing the rate of trapping of photogenerated holes (h^+)at the surface, which in turn enhances the emission intensity. We consider that the different types of chemical bonding in the molecular configuration surrounding the central Dy^{3+} cation $(OH^-, O-C-O, O-C=O)$ and its optical response is associated with the interaction of external incident electromagnetic radiation, which creates a signal. much more intense optics in AB for the TT sample. In these nanomaterials, the signals have different relative intensity observed when directly compared to each other. However, intrinsic crystalline defects must be considered in a more formal way by applying an adequate theoretical model, which is underway by our research group.

Figure 6 displayed $(\alpha hv)^2$ vs. E(hv) spectra of (a) Dy 20 and Dy 90, (b) Dy 20 TT and Dy 90 TT nanocrystals. Tauc's plot reveals an absorption edge located at range $\sim 4.66 - 5.17$eV, it is believed that may be a wide optical band gap (Eg_g) of $Dy_2(CO_3)_3$ nanomaterial. The $Dy_2(CO_3)_{3(s)}$ nanomaterial show E_g energy located at range $\sim 3.75 - 4.1$eV, have recently been reported in the literature [2,64]. A systematic analysis of the optical behavior of these nanocrystals, it is possible to divide into three regions associated with intra-electronic transitions $4fs \rightarrow 4fs$ located in the UV-Vis region at range $\sim 1.5-3.5$eV [15], fundamental transition valence band (VB) and conduction band $(CB)VB \rightarrow CB$, located at $\sim 4.66 - 5.17$ eV. The samples labeled with Dy 20 TT D and Dy 90 TT symbols show similar optical behavior at $(\alpha hv)^2$ vs. $E(hv)$ spectra spectrum. It is confirmed that both materials are Dy_2O_3 (s), so the

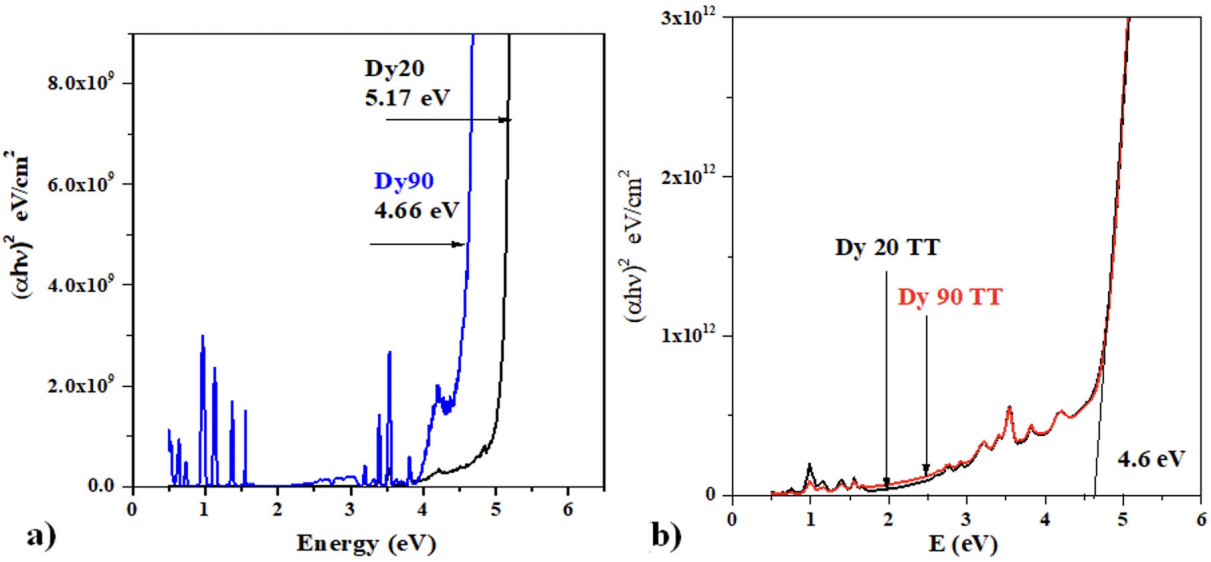

FIGURE 6. $(\alpha h\nu)^2$ vs. $E(h\nu)$ spectra of a) Dy 20 and Dy 90, b) Dy 20 TT and Dy 90 TT nanocrystals.

$E_g \sim 4.6$eV, which is very close to that reported for $Dy_2O_{3(s)}$, were attained from rare-earth oxides, with a high thermal and chemical stability [65]. The concentration of native crystalline defects (vacancies, interstices, stacking faults etc.), related transition is due to the recombination of a photogenerated hole $(h^+)$and electron (e^-)that fits a singly ionized state of the defect, such as oxygen vacancy or oxygen interstitial.

4. Conclusions

Nanomaterials containing the Dy^{3+} cation were prepared at two different temperatures of $\sim 20°C$ and $\sim 90°C \pm 2°C$, keeping the parameters constant during crystal growth and subsequent thermal treatment in an air atmosphere at $\sim 600 \pm 5°C$ during 1.0 h. The influence of changing temperature of crystal growth on the structural and optical of the material were determined. The influence of changing temperature of crystal growth on structural and optical of the material were determined. The change in optical and structural properties are systematically discussed in this document, these are associated with the TT which produces $Dy\,(CO_3)_{3(s)}$ nanocrystal. All these nanomaterials were characterized by DXR technique. It is found that Dy 20 and Dy 90 are identified in orthorhombic phase, while both samples TT present cubic phase. These nanomaterials present interesting optical properties: Transmittance (%T), Reflectivity (%R), Normalized Absorbance, real (n) and imaginary (k) parts refractive index and band gap energy (E_g). The change in optical and structural properties are systematically discussed in this document, these are associated with the TT which directly produces the $Dy_2\,(CO_3)_{3(s)} \rightarrow Dy_2O_{3(s)}$ transition. These optical properties are associated with $4fs \rightarrow 4fs$ electronic intra-transitions and E_g located at UVVis-NIR region. Using the experimental results of absorbance, the Tauc equation is applied to quantify the E_g which is located at UV-region in all these nanomaterials. These optical properties are associated with $4fs \rightarrow 4fs$ intra-electronic transitions and E_g located at UV Vis-NIR region. The optical energy E_g of the nanocrystals for direct allowed transitions are decreases with TT located at $5.1 - 4.6$ eV. The measured and calculated oscillator strengths for various electronic intra-transitions with Dy^{3+} ons, which is the highest for hypersensitive transition. This newly proposed nanomaterials may contribute to the development of photonic devices.

5. Statements and declaration

The authors declare that no funds, grants, or other support were received during the preparation of this manuscript.

1. K. N. Han, Characteristics of precipitation of rare earth elements with various precipitants, *Minerals* **10** (2020) 178.

2. M. Rahimi-Nasrabadi *et al*., Preparation of dysprosium carbonate and dysprosium oxide efficient photocatalyst nanoparticles through direct carbonation and precursor thermal decomposition, *Journal of Materials Science: Materials in Electronics* **28** (2017) 3325.

3. S. Liu *et al*., Synthesis and structure of hydrated neodymium carbonate, *Journal of crystal growth* **203** (1999) 454.

4. G. S. Goff *et al*., Synthesis and structural characterization of molecular Dy (III) and Er (III) tetra-carbonates, *Inorganic chemistry* **49** (2010) 6558.

5. M. Salavati-Niasari, J. Javidi, and F. Davar, Sonochemical syn-

thesis of $Dy_2(CO_3)_3$ nanoparticles, $Dy(OH)_3$ nanotubes and their conversion to Dy_2O_3 nanoparticles, *Ultrasonics sonochemistry* **17** (2010) 870.

6. B. Vallina *et al*., Amorphous dysprosium carbonate: characterization, stability, and crystallization pathways, *Journal of Nanoparticle Research* **15** (2013) 1.

7. P. Kim *et al*., Trends in structure and thermodynamic properties of normal rare earth carbonates and rare earth hydroxycarbonates, *Minerals* **8** (2018) 106.

8. D. Hu *et al*., Fabrication of Dy_2O_3 transparent ceramics by vacuum sintering using precipitated powders, *Magnetochemistry* **7** (2020) 6.

9. Y. Bacherikov *et al*., Thin dysprosium oxide films formed by rapid thermal annealing on porous SiC substrates, *Semiconductor physics, quantum electronics & optoelectronics* (2018) 360.

10. K. Xu *et al*., Atomic layer deposition of Gd_2O_3 and Dy_2O_3: a study of the ALD characteristics and structural and electrical properties, *Chemistry of Materials* **24** (2012) 651.

11. R. Khan *et al.*, Oxide-Based Resistive Switching Devices: Fabrication, Influence Parameters and Applications, *Journal of Materials Chemistry C* (2021).

12. S. F. Ahmed *et al.*, Green approaches in synthesising nanomaterials for environmental nanobioremediation: Technological advancements, applications, benefits and challenges, *Environmental Research* **204** (2022) 111967.

13. V. C. Téllez *et al*., Green synthesis of palladium mixed with PdO nanoparticles by chemical bath deposition, *Optical Materials* **112** (2021) 110747.

14. M. C. Portillo *et al*., White light upconversion in $NdOHCO_3$ to Nd_2O_3 nanocrystals: Structural and optical transition, *Optik* **249** (2022) 168272.

15. M. C. Portillo *et al*., Optical and structural properties of Er2O3-ErOOH powder grown by chemical bath, *Materials Letters* **151** (2015) 134.

16. N. Shanmugam *et al*., Anti-reflective coating materials: a holistic review from PV perspective, *Energies* **13** (2020) 2631

17. O. P. Moreno *et al*., Optical and structural properties of PbSIn^{3+} nanocrystals grown by chemical bath, *Thin Solid Films* **616** (2016) 800.

18. F. L. Leite *et al*., Theoretical models for surface forces and adhesion and their measurement using atomic force microscopy, *International journal of molecular sciences* **13** (2012) 12773.

19. M. M. Reif and C. Oostenbrink, Toward the correction of effective electrostatic forces in explicit-solvent molecular dynamics simulations: restraints on solvent-generated electrostatic potential and solvent polarization, *Theoretical chemistry accounts* **134** (2015) 1.

20. J.-F. Truchon *et al*., Using electronic polarization from the internal continuum (EPIC) for intermolecular interactions, *Journal of computational chemistry* **31** (2010) 811.

21. O. P. Moreno *et al*., Morphological, optical and structural analysis in CdS, CdS-$CdCO_3$ and $CdCO_3$ thin solid films grown by chemical bath, *Optik* **157** (2018) 388.

22. E. D. Shchukin and A. V. Pertsov, Thermodynamic criterion of spontaneous dispersion, *Colloid Stability* (2007) 23.

23. O. P. Moreno *et al*., Growth of Sm (OH) 3 nanocrystals by chemical bath deposition and its thermal annealing treatment to Sm_2O_3, *Optik* **135** (2017) 70.

24. O. P. Moreno *et al*., CeO_2 nanoparticles growth by chemical bath and its thermal annealing treatment in air atmosphere, *Optik* **148** (2017) 142.

25. L. S. de la Rosa *et al.*, Synthesis of holmium oxide (Ho_2O_3) nanocrystal by chemical bath deposition, *Optik* **216** (2020) 164875.

26. R. Occhipinti andW. F. Boron, Mathematical modeling of acid-base physiology, *Progress in biophysics and molecular biology* **117** (2015) 43.

27. M. Mora-Ramírez *et al*., Synthesis, characterization and optical properties of Co^{2+} doped PbS nanocrystals, *Optik* **238** (2021) 166629.

28. W. Zhou, Reversed crystal growth, *Crystals* **9** (2018) 7.

29. A. Heuer-Jungemann *et al*., The role of ligands in the chemical synthesis and applications of inorganic nanoparticles, *Chemical reviews* **119** (2019) 4819.

30. G. Meinrath and H. Takeishi, Solid-liquid equilibria of Nd^{3+} in carbonate solutions, *Journal of Alloys and Compounds* **194** (1993) 93.

31. K. N. Han, Effect of anions on the solubility of rare earth element-bearing minerals in acids, Mining, *Metallurgy & Exploration* **36** (2019) 215.

32. Y. Xia *et al.*, Shape-controlled synthesis of metal nanocrystals: simple chemistry meets complex physics?, *Angewandte Chemie International Edition* **48** (2009) 60.

33. M. Norek *et al*., Tuning of the size of Dy2O3 nanoparticles for optimal performance as an MRI contrast agent, *Journal of the American Chemical Society* **130** (2008) 5335.

34. U. Arjun *et al*., Magnetic properties of layered rare-earth oxycarbonates $Ln_2O_2CO_3$ (Ln= Nd, Sm, and Dy), *Solid State Communications* **240** (2016) 1.

35. W. Tian *et al*., A review on lattice defects in graphene: types, generation, effects and regulation, *Micromachines* **8** (2017) 163.

36. D. Gutiérrez-Argüelles *et al*., Maxwell-Boltzmann statistics applied in the study of photoluminescent emission bands in the (S)-(-)-1-(4-bromophenyl)-N-1, 2, 3, 4-(tetrahydro-1-naphthyl) methanimine organic crystals, *Optical Materials* **96** (2019) 109307.

37. M. C. Portillo *et al.*, Optical and structural analysis of the charge transfer of $Ce^{3++}\ e^{-}$ –¿ Ce^{4+} ion in the cerium oxide (CeO_2), *Optik* **248** (2021) 168178.

38. I. Galanakis, N. Papanikolaou, and P. Dederichs, Applicability of the broken-bond rule to the surface energy of the fcc metals, *Surface science* **511** (2002) 1.

39. J. Poater, M. Duran, and M. Solá, Aromaticity determines the relative stability of kinked vs. straight topologies in polycyclic aromatic hydrocarbons, Frontiers in chemistry (2018) 561.

40. A. Tok *et al*., Homogeneous precipitation of Dy_2O_3 nanoparticles- effects of synthesis parameters, *journal of Nanoscience and Nanotechnology* **7** (2007) 907.

41. R. Tran *et al.*, Surface energies of elemental crystals, *Scientific data* **3** (2016) 1.
42. P. Zhang, T. Wu, and K. Huang, Identification of Active Surface Species in Molten Carbonates Using in situ Raman Spectroscopy, *Frontiers in Energy Research* (2021) 143.
43. R. P. Turcotte, J. O. Sawyer, and L. Eyring, *Rare earth dioxymonocarbonates and their decomposition, inorganic Chemistry* **8** (1969) 238.
44. K. Nakamoto, *Infrared and Raman spectra of inorganic and coordination compounds, part B: applications in coordination, organometallic, and bioinorganic chemistry* (John Wiley & Sons, 2009).
45. M. Chandrasekhar *et al*., Structural and phase dependent thermo and photoluminescent properties of $Dy(OH)_3$ and Dy_2O_3 nanorods, *Materials Research Bulletin* **47** (2012) 2085.
46. K. Gopinath *et al.*, One-pot synthesis of dysprosium oxide nano-sheets: antimicrobial potential and cyotoxicity on a549 lung cancer cells, *Journal of Cluster Science* **28** (2017) 621.
47. N. D. Sharma *et al*., Pressure-induced anomalous phase transformation in nano-crystalline dysprosium sesquioxide, *Journal of Raman Spectroscopy* **42** (2011) 438.
48. Y. Jinqiu *et al*., Raman spectra of RE_2O_3 (RE= Eu, Gd, Dy, Ho, Er, Tm, Yb, Lu, Sc and Y): laser-excited luminescence and trace impurity analysis, *Journal of Rare Earths* **32** (2014) 1.
49. R. Khokhra *et al*., Visible and UV photo-detection in ZnO nanostructured thin films via simple tuning of solution method, *Scientific reports* **7** (2017) 1.
50. M. Nelson, *Characterization of SnxSey/SnO_2-Ni prepered by spray pyrolysis for photovoltaic application*, Ph.D. thesis, Kenyatta University (2016).
51. S. H. Jaafar *et al.*, Influence of Calcination Temperature on Crystal Growth and Optical Characteristics of Eu^{3+} Doped ZnO/Zn_2SiO_4 Composites Fabricated via Simple Thermal Treatment Method, *Crystals* **11** (2021) 115.
52. A. Ichoja *et al*., Physical, structural and optical studies on magnesium borate glasses doped with dysprosium ion, *Journal of Rare earths* **36** (2018) 1264.
53. D. J. Jovanovi'c *et al*., Synthesis, structure and spectroscopic properties of luminescent $GdVO_4$: Dy_{3+} and $DyVO_4$ particles, *Optical Materials* **76** (2018) 308.
54. M. Almessiere *et al*., Impact of Dy_2O_3 nanoparticles additions on the properties of porous YBCO ceramics, *Journal of Materials Science: Materials in Electronics* **30** (2019) 17572.
55. V. Olifirenko *et al*., Potential applicability of polyethyleneimine PEI-coated Eu_2O_3 and Dy_2O_3 nanoparticles for contrast enhancement in computed tomography, *Nano Express* **2** (2021) 010022.
56. O. Bagi Aljewaw *et al*., Impact of Dy_2O_3 substitution on the physical, structural and optical properties of lithium-aluminium-borate glass system, *Applied Sciences* **10** (2020) 8183.
57. A. Shafiqa, A. A. Aziz, and B. Mehrdel, Nanoparticle optical properties: Size dependence of a single gold spherical nanoparticle, *In Journal of Physics: Conference Series*, **1083** (2018) 012040.
58. A. M. Babu *et al.*, Spectroscopic and photoluminescence properties of Dy^{3+} -doped lead tungsten tellurite glasses for laser materials, *Journal of alloys and compounds* **509** (2011) 457.
59. M. Mhareb, *et al*., Effect of Dy_2O_3 impurities on the physical, optical and thermoluminescence properties of lithium borate glass, *Journal of Luminescence* **177** (2016) 366.
60. N. Deopa and A. Rao, Photoluminescence and energy transfer studies of Dy^{3+} ions doped lithium lead alumino borate glasses for w-LED and laser applications, *Journal of Luminescence* **192** (2017) 832.
61. M. Chandrasekhar *et al.*, Comparison of structural and luminescence properties of Dy_2O_3 nanopowders synthesized by co-precipitation and green combustion routes, *Materials Research Bulletin* **55** (2014) 237.
62. N. Arleth *et al*., Molecular Polyarsenides of the Rare-Earth Elements, *Angewandte Chemie International Edition* **55** (2016) 1557.
63. G. Ahuja and G. Arora, Study of Electronic Properties of Dy_2O_3 using First Principles Calculations, *International Journal of Pure and Applied Physics* **13** (2017) 123.
64. F.-C. Chiu, Electrical characterization and current transportation in metal/Dy_2O_3/ Si structure, *Journal of Applied Physics* **102** (2007) 044116.